JOURNAL OF MATERIALS SCIENCE 24 (1989) 4246–4252

The microstructure of extruded Fe–Al

P. R. MUNROE, I. BAKER,
Thayer School of Engineering, Dartmouth College, Hanover, New Hampshire 03755, USA.

Five FeAl alloys, whose compositions span the range 34 to 51 at.% Al, were extruded at 1273 K, re-extruded at 1023 K and their deformation structures examined by transmission electron microscopy. The incidence of ⟨1 1 1⟩ slip, compared with ⟨0 0 1⟩ slip, was found to increase as Fe–Al became more iron-rich, confirming previous results, in a similar study: some of the ⟨1 1 1⟩ dislocations were found to be present in the form of dipoles. In the most aluminium-rich alloy square ⟨0 0 1⟩ prismatic dislocation loops, planar defects and $FeAl_2$ particles were observed.

1. Introduction

Fe–Al is a B2-structured phase which exists over a wide range of composition (34 to 51 at.% Al). Previous studies of the operative slip vector as a function of composition and temperature have yielded conflicting results. Umakoshi and Yamagauchi [1] examined the slip mode, by two-surface slip trace analysis, of three single crystal iron-rich alloys (47.2, 48.1 and 49.2 at.% Al), and suggested that at high temperatures there was a transition in slip direction from ⟨1 1 1⟩ to ⟨1 0 0⟩ and that the transition temperature increased with increasing aluminium content. However, Mendiratta, Kim and Lipsitt [2], who examined a series of five iron-rich polycrystalline alloys (spanning the composition 34 to 50 at.% Al) by transmission electron microscopy, observed a decrease in the ⟨1 1 1⟩ to ⟨1 0 0⟩ slip transition temperature as the aluminium content increased. A trend also noted by Baker and Gaydosh on examination of two iron-rich Fe–Al alloys [3]. Mendiratta *et al* [2] also observed dislocation pairs in the most iron-rich alloy, which they indicated to be superlattice partials.

This paper part of a larger study on Fe–Al and Ni–Al, presents the results of a transmission electron microscope examination on a range of extruded Fe–Al alloys covering the composition range 34 to 51 at.% Al.

2. Experimental procedures

Five Fe–Al alloys, whose compositions span the B2 phase field, were cast into ingots (diameter 50 mm, length 150 mm). Sections from each alloy, 100 mm long, were canned in 75 mm outside diameter stainless steel and extruded at 1273 K at a 7 : 1 area reduction ratio. Sections, 100 mm long, of the extruded material were recanned in mild steel and re-extruded at 1023 K at a 6 : 1 area reduction ratio and then slowly cooled in sand. The grain sizes and hardnesses of each alloy after both extrusions are given in Table I. From the table, it appears that the hardness decreases as Fe–Al becomes increasingly iron-rich and as the grain size decreases. It should be noted that the hardness of Fe–Al is weakly dependent upon grain size [4], and it has also been shown to be dependent upon cooling rate [5].

Thin foils were prepared from all the alloys as described elsewhere [6], and examined in either a JEOL 100CX operated at 100 kV or a JEOL 2000FX operating at 200 kV furnished with a Tracor Northern 5500 Series II X-ray microanalysis unit.

3. Results

Transmission electron microscopy of the alloys after their initial extrusion at 1273 K revealed a microstructure of recrystallized equiaxed grains displaying evidence of a ⟨1 1 1⟩ texture. The dislocations within these alloys were of ⟨0 0 1⟩ Burgers' vector and often arranged in networks (Fig. 1). The exception being the alloy with the lowest aluminium content Fe–34 at.% Al, where both ⟨1 1 1⟩ and ⟨0 0 1⟩ dislocations were observed. Fig. 2 shows ⟨0 0 1⟩ dislocations labelled *a* together with ⟨1 1 1⟩ dislocations labelled *b*, many of the ⟨1 1 1⟩ dislocation were in sub-boundaries, which indicates that diffusion-assisted processes, such as climb, were in operation during extrusion.

The predominance of ⟨1 0 0⟩ slip after the first extrusion is not unexpected as the extrusion temperature employed was 1273 K, and, as earlier noted, elevated temperatures favour ⟨0 0 1⟩ slip. However, the presence of ⟨1 1 1⟩ slip in the most iron-rich alloy indicates that the temperature of transition from ⟨1 1 1⟩ slip to ⟨1 0 0⟩ increases as the intermetallic becomes more iron-rich.

The dislocations present after the second extrusion at 1023 K were also examined by transmission electron microscopy. Again the structure consisted of recrystallized, equiaxed grains displaying a ⟨1 1 1⟩ texture. The dislocations in Fe–50 at.% Al were found to be exclusively ⟨1 0 0⟩ in nature: for example, in Fig. 3, the dislocations labelled *a* are in contrast when $\boldsymbol{g} = 10\bar{1}$ and $01\bar{1}$, but show invisibility or weak contrast* when $\boldsymbol{g} = 020$ and $-\bar{1}10$, indicating a [001]

*Fe–Al is strongly anisotropic. The Zener anisotropic factor, *A*, of stoichiometric Fe–Al is 2.94 [7], and there is often residual contrast even when a dislocation is viewed under conditions which satisfy the $\boldsymbol{g} \cdot \boldsymbol{b} = 0$ invisibility criterion.

0022–2461/89 $03.00 + .12

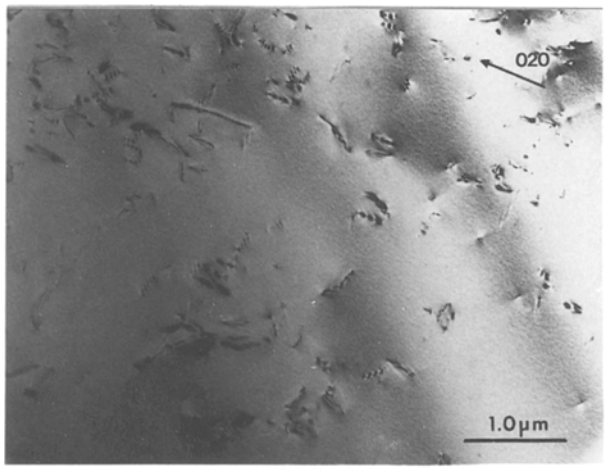

Figure 1 Transmission electron micrograph of Fe–45 at.% Al extruded at 1273 K. Diffracting vector as shown, beam direction close to [0 0 1].

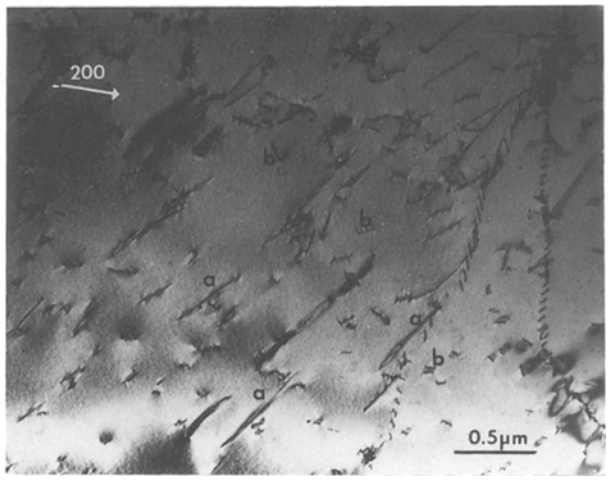

Figure 2 Transmission electron micrograph of Fe–34 at.% Al extruded at 1273 K, showing both ⟨0 0 1⟩ dislocations, marked *a* and ⟨1 1 1⟩ dislocations marked *b*. Diffracting vector as shown, beam direction close to [0 1 1].

Burgers' vector. The line directions of these dislocations was found to be $[0\bar{1}1]$, which indicates that they glide on {1 0 0} planes. The residual contrast is much stronger for $\boldsymbol{g} = \bar{1}10$ than $\boldsymbol{g} = 020$ because although $\boldsymbol{g} \cdot \boldsymbol{b} = 0$ for both diffraction vectors $\boldsymbol{g} \cdot (\boldsymbol{b} \times \boldsymbol{u})$ is zero only for $\boldsymbol{g} = 020$ [8]. Since the line direction is oriented 45° away from the Burgers' vector these dislocations are mixed in character, which is in contrast to previous studies which have shown that ⟨0 0 1⟩ dislocations in Fe–Al are pure edge in character and glide on {1 1 0} planes [2, 3]. However, inverse Wulff plot calculations on the stability of orientation of ⟨0 0 1⟩ {1 0 0} dislocations in Ni–Al, which exhibits a similar degree of anisotropy to FeAl, showed that the stability of ⟨0 0 1⟩ {1 0 0} dislocations was greatest for 45° mixed dislocations [9].

Fig. 4 shows a series of micrographs from Fe–34 at.% Al, analysis of the dislocations present indicated that they all have a ⟨1 1 1⟩ Burgers' vector: dislocations marked *a* show contrast consistent with the specific Burgers' vector [1 1 1]. Examination of those alloys with intermediate compositions, for example Fe–40 at.% Al in Fig. 5, revealed the existence of both ⟨0 0 1⟩ and ⟨1 1 1⟩ dislocations; with the incidence of ⟨1 1 1⟩ slip increasing with increasing iron content.

Paired defects were observed in those alloys where ⟨1 1 1⟩ dislocations were present. The incidence of these pairs increased as the alloys became more iron-rich, presumably with the increased incidence of ⟨1 1 1⟩ slip. In order to determine whether these pairs were dislocation dipoles or superlattice dislocations, some were imaged using both $+\boldsymbol{g}$ and $-\boldsymbol{g}$ two-beam diffraction conditions. The spacing between two superlattice partials (which are of like sign) is independent of the sign of $\boldsymbol{g}$, but the spacing between two dislocation dipoles, which are of opposite sign, should change when $\boldsymbol{g}$ is reversed [10]. In Fig. 6, for example, the dislocations marked *a* were imaged using $+\boldsymbol{g}$ and $-\boldsymbol{g}$ and it can be clearly seen that the spacing of this dislocation pair changes when the sign of $\boldsymbol{g}$ is changed, indicating that the paired defects are dislocation dipoles rather than superlattice pairs.

Attempts to resolve individual ⟨1 1 1⟩ dislocations into a/2 ⟨1 1 1⟩ partials, using weak-beam imaging, were unsuccessful, indicating a very close spacing of the partials, although, Ray *et al.* [11] measured a 5 nm spacing between ⟨1 1 1⟩ dislocation superlattice partials in Fe–35 at.% Al deformed at room temperature.

In the aluminium-rich alloy, Fe–51 at.% Al, several other features were observed. First, a small number of planar faults, consisting of dislocations bounding displacement fringes, were observed (Fig. 7). These fringes were too small and infrequently observed to allow an unambiguous determination of their nature.

Second, square dislocation loops were found but only in the thicker regions of the foil, suggesting that they were able to glide out of thinner regions of the foil due to image forces [12]. Fig. 8 shows a series of micrographs of one of these square dislocation loops imaged under a series of different operating reflections: the two horizontal sides are marked *a* and the two vertical sides *b*. Trace analysis was used to determine the line directions, $\boldsymbol{u}$, of the dislocations and it was

TABLE I Nominal compositions, grain sizes and hardnesses of FeAl alloys after extrusion

Composition (at.%)	First extrusion		Second extrusion	
	Grain Size (μm)	Hardness (kg mm^{-2})	Grain Size (μm)	Hardness (kg mm^{-2})
Fe–34Al	82	255 ± 8	46	265 ± 5
Fe–40Al	80	279 ± 4	30	308 ± 9
Fe–45Al	72	295 ± 8	30	407 ± 10
Fe–50Al	88	491 ± 14	26	552 ± 12
Fe–51Al	96	530 ± 8	28	601 ± 9

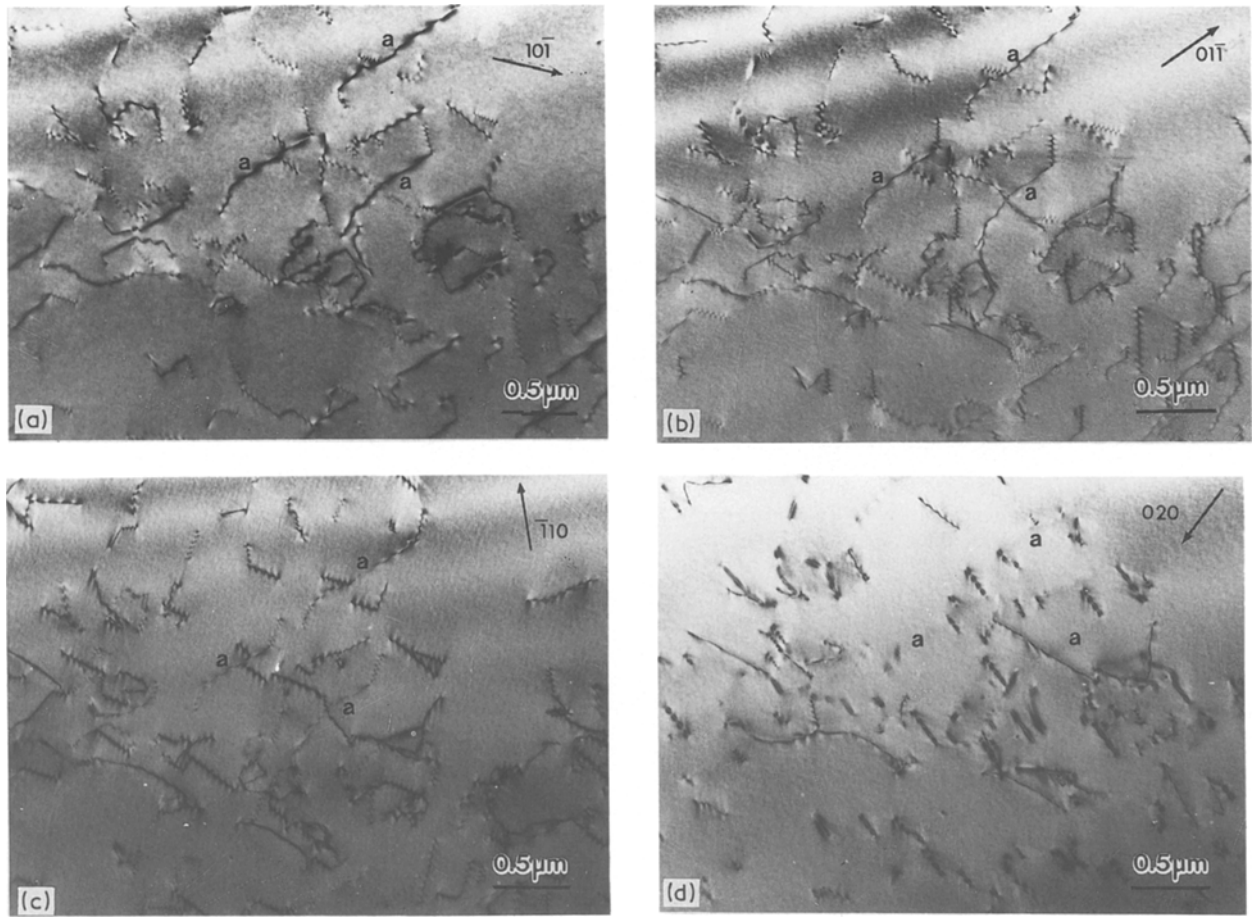

Figure 3 Dislocations in double extruded Fe–50 at.% Al, the dislocations marked *a* have an [0 0 1] Burgers' vector. Diffracting vectors as shown, (a), (b) and (c) are near to [1 1 1], (d) is near to [101].

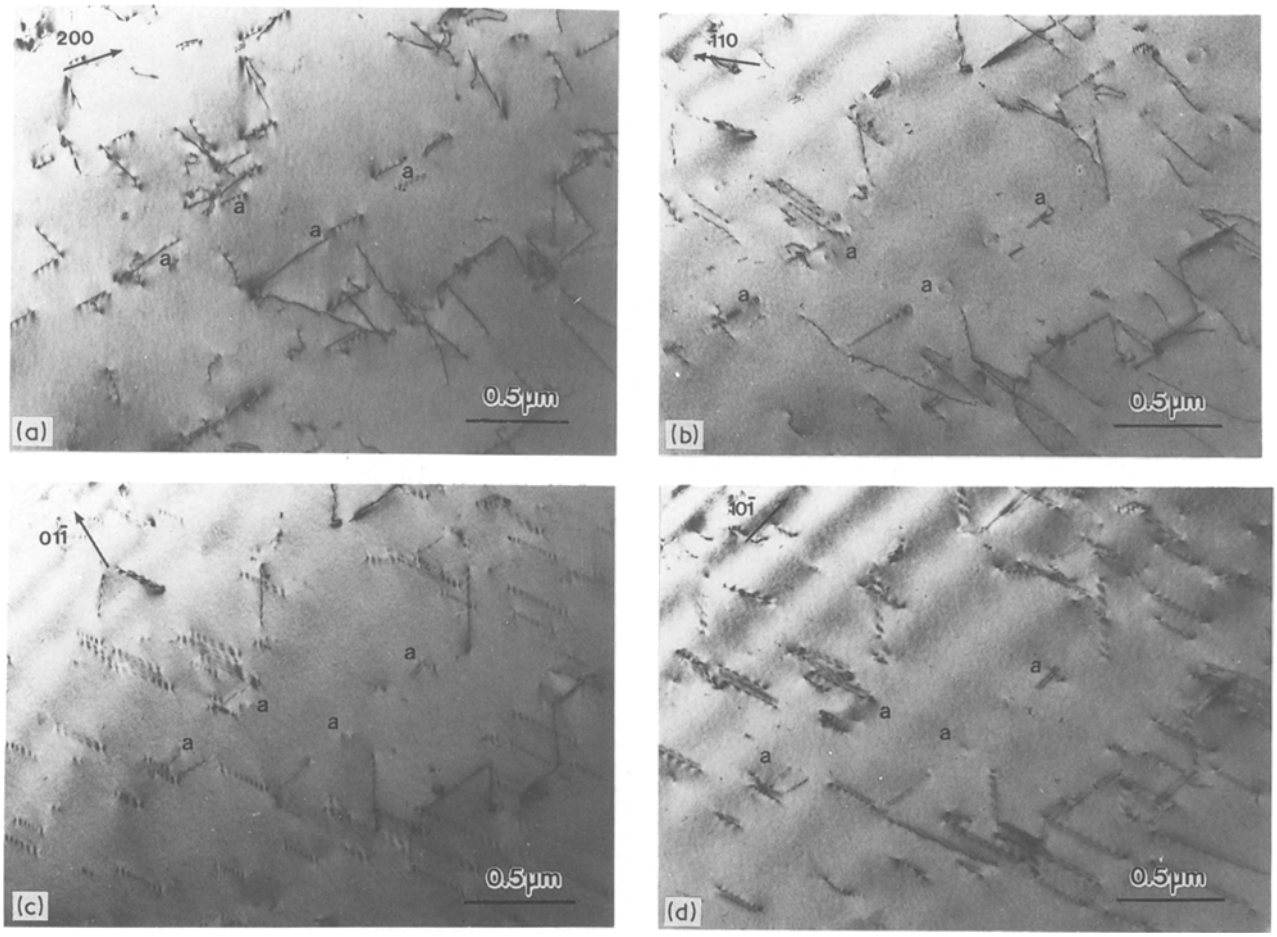

Figure 4 Dislocations in double extruded Fe–34 at.% Al, the dislocations marked *a* have the Burgers' vector [1 1 1]. Diffracting vectors as shown, (a) is near to [0 0 1], (b), (c) and (d) are near to [1 1 1].

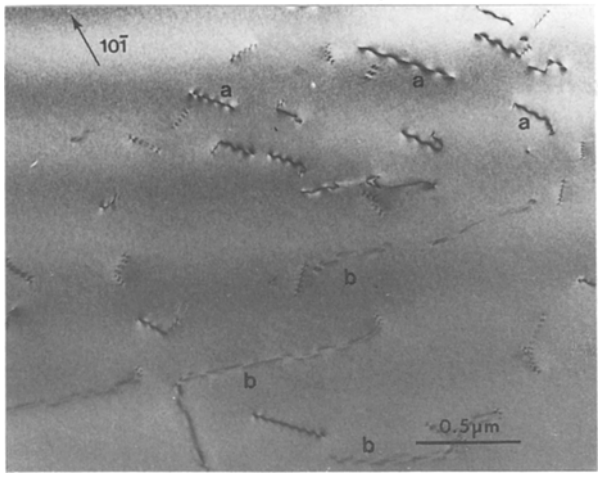

Figure 5 Dislocations in double extruded Fe–40 at.% Al, the dislocations marked *a* have a ⟨0 0 1⟩ Burgers' vector and those marked *b* have a ⟨1 1 1⟩ Burgers' vector. Diffracting vector as shown, beam direction close to [1 1 1].

must be a [0 0 1] rather than $\frac{1}{2}a$[0 0 1], since a $\frac{1}{2}a$[0 0 1] shear would result in the presence of fault contrast within the loop for all the diffracting conditions shown in Fig. 8. Interestingly, when the network is imaged with a reflection where $\boldsymbol{g} \cdot \boldsymbol{b} = 0$ but $\boldsymbol{g} \cdot (\boldsymbol{b} \times \boldsymbol{u}) \neq 0$, for example when $\boldsymbol{g} = 1\bar{1}0$, the contrast from the loop appears as a weak double image, but with no contrast observed in two of the corners. It is possible that the corner regions have a line direction of ⟨1 1 0⟩ and therefore this portion of the loop satisfies both the $\boldsymbol{g} \cdot \boldsymbol{b} = 0$ and $\boldsymbol{g} \cdot (\boldsymbol{b} \times \boldsymbol{u}) = 0$ invisibility criteria. Similar loops (and planar fringes) were observed by Baker and Crimp [13] in near-stoichiometric Fe–Al containing 2 at.% B (Fig. 9). The opposite corners of the loop were again invisible when imaged under conditions where both invisibility criteria were satisfied for the ⟨1 0 0⟩ edges.

Third, small particles, ≈ 50 nm diameter, were observed at the grain boundaries of Fe–51 at.% Al

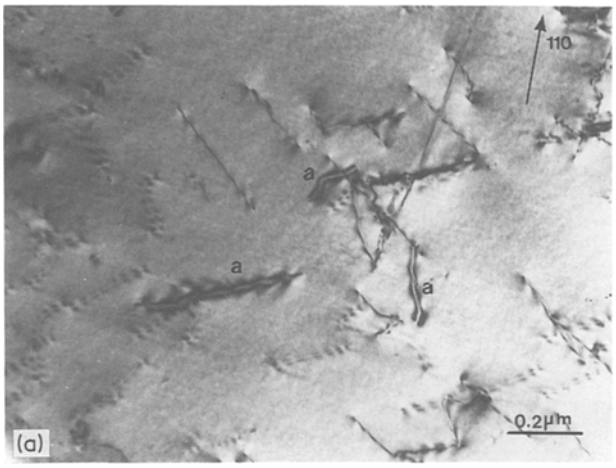

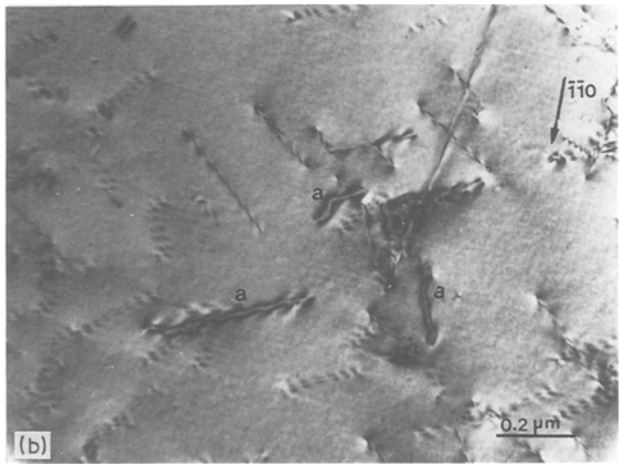

Figure 6 Dislocation dipole in double extruded Fe–34 at.% Al, the dipoles marked *a* are imaged using diffracting vectors (a) 1 1 0 and (b) $\bar{1}\bar{1}$0, beam direction close to [$\bar{1}$1$\bar{1}$]. The spacing between these dislocations changes as $\boldsymbol{g}$ is reversed indicating a dislocation dipole.

found that $\boldsymbol{u}_a = [0\,1\,0]$ and $\boldsymbol{u}_b = [1\,0\,0]$. Thus the loop lies on the (0 0 1) plane. The dislocation contrast from this loop is summarized in Table II, from which it can be deduced that all four sides are edge dislocations with a Burgers' vector of [0 0 1]. The Burgers vector

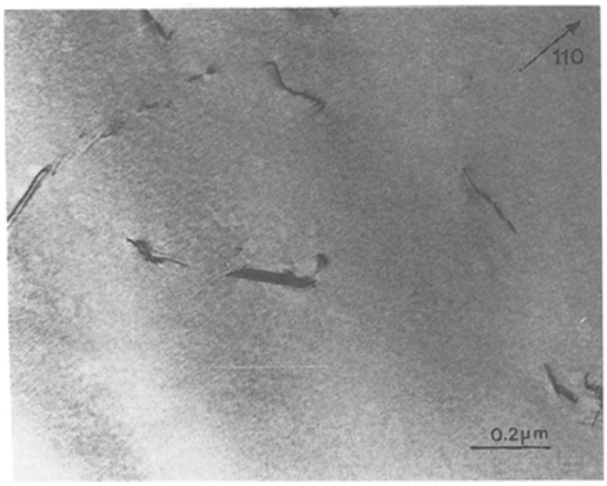

Figure 7 Planar fringes in double extruded Fe–51 at.% Al. Diffracting vector as shown, beam direction close to [1-1 1].

(Fig. 10). X-ray microanalysis of these particles indicated a higher aluminium content than the surrounding matrix (Fig. 11) and quantitative analysis indicated a composition close to $FeAl_2$. Since the composition of this alloy lies close to the FeAl–FeAl + $FeAl_2$ phase boundary, the observation of $FeAl_2$ particles is not unreasonable.

4. Discussion

The increased incidence of ⟨1 1 1⟩ slip in Fe–Al as it becomes more iron-rich is in agreement with the results of Mendiratta *et al.* [2] but not with those of Umakoshi and Yamagauchi [1]. This increase in

TABLE II A summary of the dislocation contrast displayed by the square dislocation network shown in Fig. 8.

Operating reflection	Beam direction	Contrast from *a*	Contrast from *b*
$\bar{1}$01	1 1 1	in	in
0 2 0	1 0 3	invisible	double
2 0 0	0 0 1	double	invisible
1$\bar{1}$0	1 1 3	weak double	weak double
1 1 0	1$\bar{1}$1	weak double	weak double
0 1 1	1$\bar{1}$1	in	in

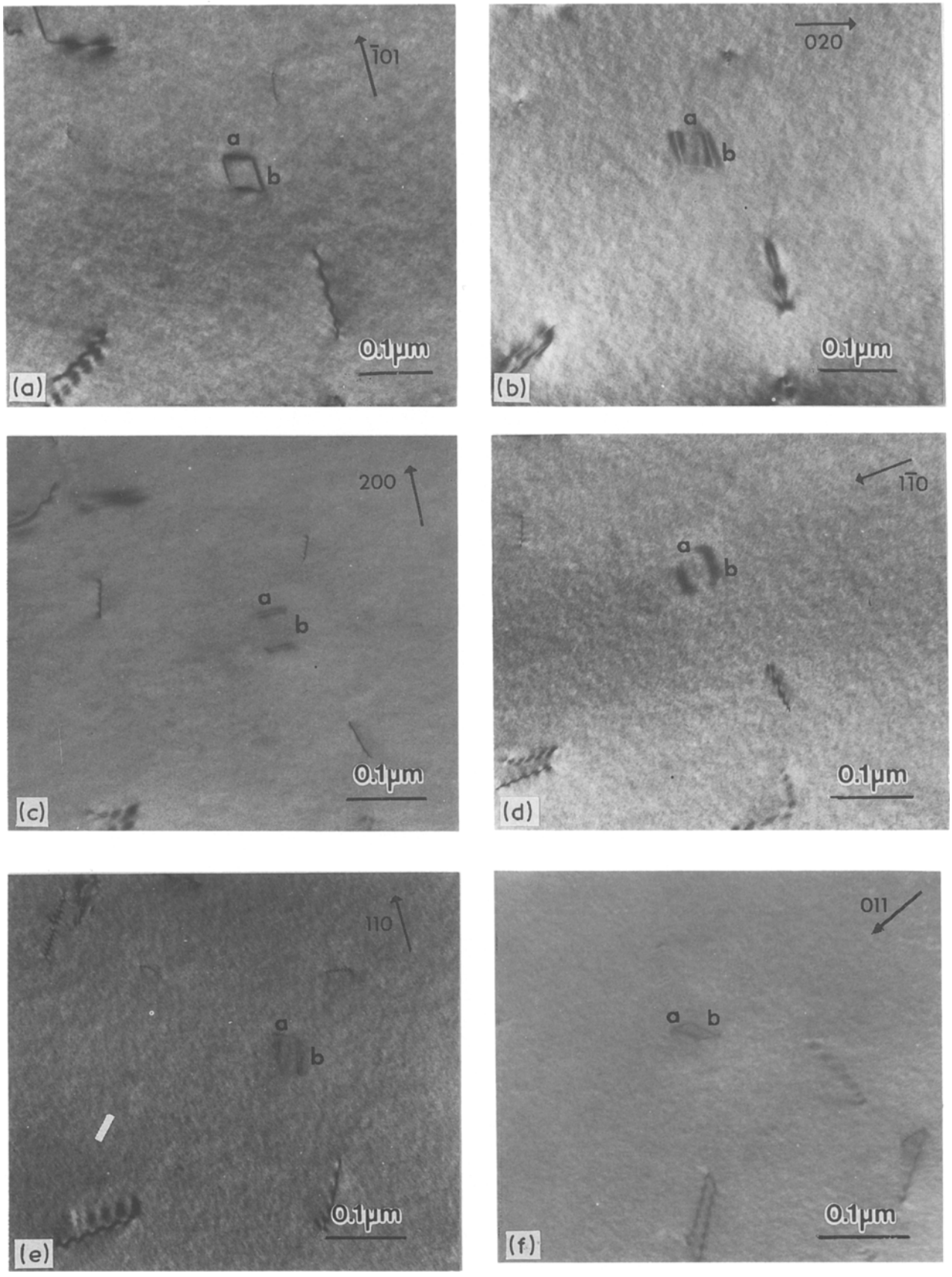

Figure 8 Square dislocation loop in double extruded Fe–51 at.% Al, the sides are marked *a* and *b*, the contrast displayed by this loop is summarized in Table II. Diffracting vectors as shown, beam directions near (a) [1 1 1], (b) [1 0 3], (c) [0 0 1], (d) [1 1 3], (e) and (f) [$1\bar{1}1$]. (Note the image has been rotated to help framing.)

$\langle 1\,1\,1\rangle$ slip may be rationalized by considering the effect of composition on antiphase boundary energy, APB. One would expect the APB energy to decrease as the iron concentration increases, since the alloy is becoming less ordered. Thus increasing the iron concentration would lower the energy of $a\langle 1\,1\,1\rangle$ dislocation, which consists of two $\frac{1}{2}a\langle 1\,1\,1\rangle$ partials separated by an APB, with respect to the energy of a perfect $a\langle 1\,0\,0\rangle$ dislocation, thus enhancing the stability of $\langle 1\,1\,1\rangle$ slip.

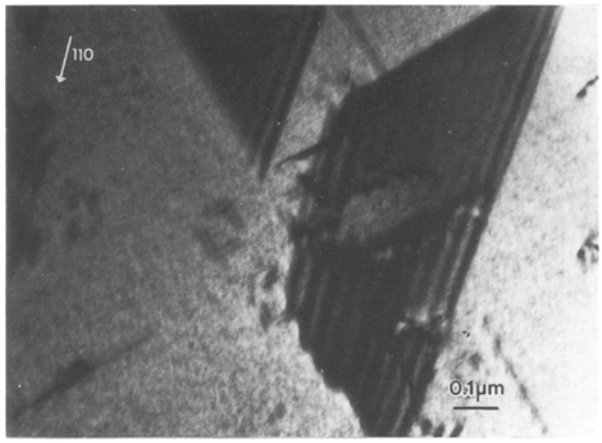

Figure 9 Square dislocation loop in Fe–50 at.% Al–2 at.% B, contrast consists of double image of loop except at opposite corners where no contrast is observed. Diffracting vector as shown, beam direction near [0 0 1].

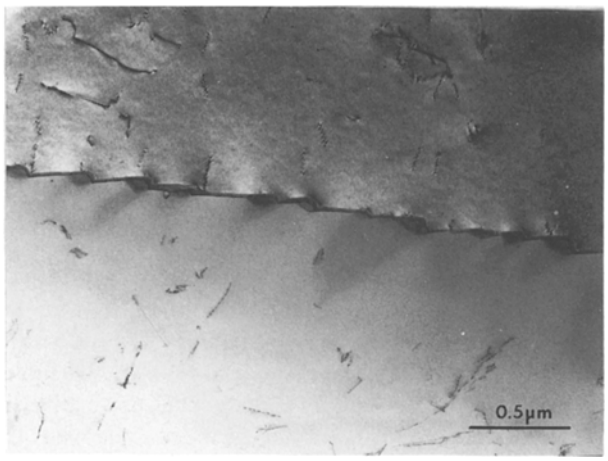

Figure 10 Transmission electron micrograph of $FeAl_2$ particles at the grain boundary in double extruded Fe–51 at.% Al.

The dislocation dipoles observed in the alloys studied here were ⟨1 1 1⟩ dislocations, which is in contrast to the ⟨0 0 1⟩ dislocation dipoles reported by Mendiratta *et al.* [2] in Fe–48 at.% Al. However, the evidence presented by the latter in support of ⟨0 0 1⟩ dislocation dipoles is not convincing. The micrograph they present in Fig. 4 [1] has an operating reflection $\boldsymbol{g} = 002$, which should give no contrast, weak contrast or double images for two-thirds of the ⟨0 0 1⟩ dislocations, which is not the case. Although dislocations dipoles were commonly observed in the Fe–Al alloys studied here, they are not seen in the B2-structured intermetallic Ni–Al, where the preferred slip system involves glide of ⟨0 0 1⟩ dislocations [14]. This is presumably because ⟨0 0 1⟩ screw dislocations are not confined to any specific plane and so they are able to cross-slip around any obstacles. In comparison, ⟨1 1 1⟩ dislocations in Fe–Al are confined to glide on specific planes, which may lead to interactions with obstacles and dipole formation.

Square prismatic dislocation loops on {1 0 0} with a ⟨1 0 0⟩ Burgers' vector were only observed in the aluminium-rich alloy. Similar loops have also been observed in single crystal aluminium-rich Ni–Al when slowly cooled from 1448 K [15–18]. The mechanism of formation of the loops in Ni–Al was suggested to be through the aggregation of compositional vacancies on the nickel sublattice, arising from the deficiency in nickel. The lower density of loops in Fe–Al compared with the number observed in Ni–Al may have been due to the grain boundaries in the Fe–Al acting as sinks for both thermal vacancies and impurities. In Ni–Al these loops emanated from sources, thought to be aluminium silicate impurity particles [17]. However, in the Fe–Al alloy examined here, no particle, which may have acted as a source, could be seen at the centre of the loop. Thus the source of the loops is

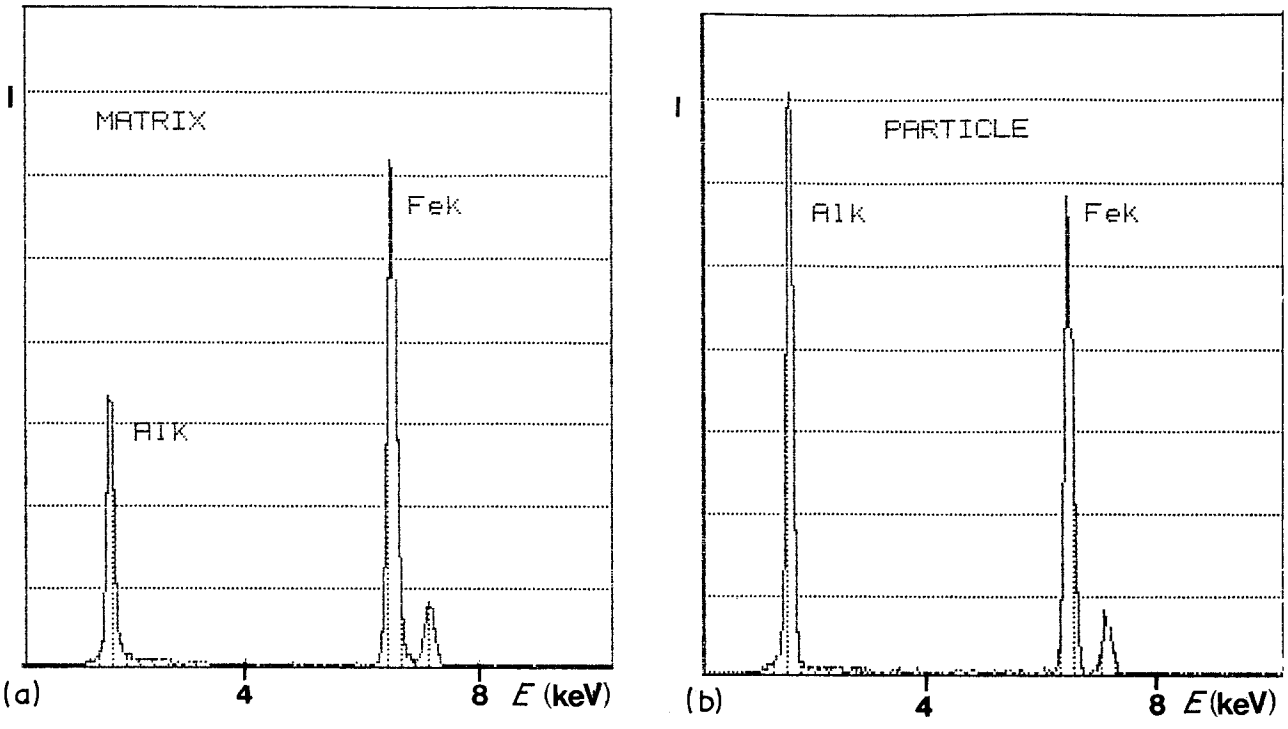

Figure 11 EDS spectra taken from (a) the matrix (b) grain boundary particle in Fe–51 at.% Al.

unknown. The square shape of the loops with edges along ⟨1 0 0⟩ directions is presumably due to the elastic anisotropy of Fe–Al, where the dislocation self energy is lowest for dislocations along the cube axes. Similar prismatic loops have been observed in copper-rich β-brass [19].

The planar fringes were also only observed in the aluminium-rich alloy. Clearly, if these planar defects arose from impurities, similar to those fringes observed by Baker and Gaydosh [6], then they would also have been observed in stoichiometric and iron-rich Fe–Al since all alloys were made from the same starting materials. It seems likely that these planar fringes are analogous to the fringes observed in aluminium-rich Ni–Al by Ball [20]. In that case, the fringes were suggested to be due to platelets of aluminium atoms sandwiched between layers of nickel vacancies, formed as a means of accommodating the excess aluminium atoms.

5. Conclusions

Transmission electron microscopy of a range of extruded Fe–Al alloys indicated that the incidence of ⟨1 1 1⟩ slip in Fe–Al increased as the alloy became more iron-rich confirming previous work by Mendiratta *et al.* [2] ⟨1 1 1⟩ dislocation dipoles, formed probably during extrusion, were observed in all alloys, but ⟨1 1 1⟩ partial dislocations could not be resolved, even using weak beam imaging. Several features were only observed in aluminium-rich Fe–Al namely square ⟨0 0 1⟩ dislocation loops, probably formed through vacancy aggregation; planar defects, thought to be layers of aluminium atoms; and $FeAl_2$ particles.

Acknowledgements

The authors gratefully acknowledge F. D. Lemkey of the United Technologies Research Center for providing the ingots and D. J. Gaydosh and J. D. Whittenberger of the NASA Lewis Research Center for extruding the ingots. This work is supported by the Division of Materials Sciences, Office of Basic Energy Sciences of the United States Department of Energy through grant DE-FG02-87ER45311. The use of the Dartmouth College Electron Microscope Center is also acknowledged.

References

1. Y. UMAKOSHI and M. YAMAGAUCHI, *Phil. Mag. A* **44** (1980) 711.
2. M. G. MENDIRATTA, H.-M. KIM and H. A. LIPSITT, *Metall. Trans.* **15A** (1984) 395.
3. I. BAKER and D. J. GAYDOSH, *Mater. Sci. Eng.* **96** (1987) 147.
4. D. WEBER, M. MEUTAIN, D. PARIS, A. FORDEUX and P. LESBATS, *J. Physique* **38** (1977) 7.
5. B. SCHMIDT, P. NAGPAL and I. BAKER, Proceedings MRS, **131** (1989) 755.
6. I. BAKER and D. J. GAYDOSH, *Phys. Status Solidi.* **96** (1986) 185.
7. D. I. POTTER, *Mater. Sci. Eng.* **5** (1970) 201.
8. P. B. HIRSCH, A. HOWIE, R. B. NICHOLSON, D. W. PASHLEY and M. J. WHELAN, in "Electron Microscopy of Thin Crystals", (Krieger, Malabar, Florida, 1977) p. 178.
9. D. L. YANEY, A. R. PELTON and W. D. NIX, *J. Mater. Sci.* **21** (1986) 2083.
10. G. THOMAS and M. J. GORINGE, in "Transmission Electron Microscopy of Materials", (Wiley, New York, 1979), p. 157.
11. I. L. RAY, R. C. CRAWFORD and D. J. H. COCKAYNE, *Phil. Mag.* **21** (1970) 1027.
12. J. P. HIRTH and J. LOTHE, in "Theory of Dislocations" (Wiley, New York, 1982), p. 86.
13. M. CRIMP and I. BAKER, unpublished research.
14. A. BALL and R. E. SMALLMAN, *Acta Metall.* **14** (1966) 1517.
15. T. C. TISONE, G. W. MARSHALL and J. O. BRITTAIN, *J. App. Phys.* **39** (1968) 3714.
16. G. W. MARSHALL and J. O. BRITTAIN, *Metall. Trans.* **6A** (1975) 921.
17. *Idem., ibid.* **7A** (1976) 101.
18. S. V. RINNOVATORE and N. BROWN, *Trans. AIME* **239** (1967) 225.
19. S. G. CUPCHALK and N. BROWN, *Acta Metall.* **15** (1967) 847.
20. A. BALL, *Phil. Mag.* **20** (1969) 113.

Received 20 September 1988
and accepted 13 February 1989